



# Direct, operando observation of the bilayer solid electrolyte interphase structure: Electrolyte reduction on a non-intercalating electrode

Christopher H. Lee<sup>a</sup>, Joseph A. Dura<sup>b</sup>, Amy LeBar<sup>a</sup>, Steven C. DeCaluwe<sup>a,\*</sup>

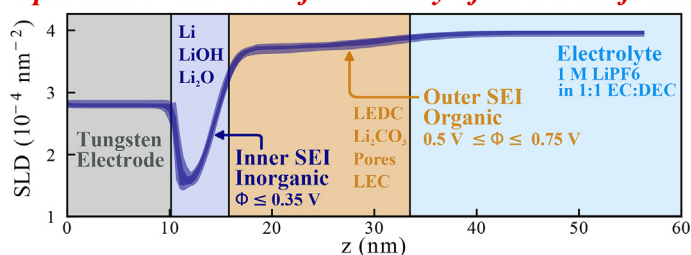
<sup>a</sup> Department of Mechanical Engineering, Colorado School of Mines, Golden, CO 80401, USA

<sup>b</sup> NIST Center for Neutron Research, Gaithersburg, MD, 20899, USA



## GRAPHICAL ABSTRACT

### Operando Neutron Reflectometry of Li-ion half-cell



## ARTICLE INFO

### Keywords:

Li ion battery  
SEI  
In operando diagnostics  
Non-intercalating electrode  
Neutron reflectometry  
Electrochemical quartz crystal microbalance

## ABSTRACT

The solid electrolyte interphase (SEI) remains a central challenge to lithium-ion battery durability, in part due to poor understanding of the basic chemistry responsible for its formation and evolution. In this study, the SEI on a non-intercalating tungsten anode is measured by operando neutron reflectometry and quartz crystal microbalance. A dual-layer SEI is observed, with a 3.7 nm thick inner layer and a 15.4 nm thick outer layer. Such structures have been proposed in the literature, but have not been definitively observed via neutron reflectometry. The SEI mass per area was 1207.2 ng/cm<sup>2</sup>, and QCM provides insight into the SEI formation dynamics during a negative-going voltage sweep and its evolution over multiple cycles. Monte Carlo simulations identify SEI chemical compositions consistent with the combined measurements. The results are consistent with a primarily inorganic, dense inner layer and a primarily organic, porous outer layer, directly confirming structures proposed in the literature.

Further refinement of techniques presented herein, coupled with additional complementary measurements and simulations, can give quantitative insight into SEI formation and evolution as a function of battery materials and cycling conditions. This, in turn, will enable scientifically-guided design of durable, conductive SEI layers for Li-ion batteries for a range of applications.

## 1. Introduction

Despite their ubiquity in energy storage for diverse applications, commercial implementation of lithium-ion batteries (LIB) remains

constrained by a number of durability and safety issues. Central to many of these issues are degradation reactions at the anode-electrolyte interface. At low anode electric potentials, electrolyte reduction products form interfacial layers on the anode surface, such as the solid

\* Corresponding author.

E-mail address: [decaluwe@mines.edu](mailto:decaluwe@mines.edu) (S.C. DeCaluwe).

<https://doi.org/10.1016/j.jpowsour.2018.11.093>

Received 1 August 2018; Received in revised form 20 November 2018; Accepted 28 November 2018

Available online 14 December 2018

0378-7753/ © 2018 Elsevier B.V. All rights reserved.

electrolyte interface (SEI) [1,2]. The SEI is ionically conductive but electrically resistive, and is therefore theoretically self-passivating and prevents further electrolyte degradation. However, continued SEI growth and electrolyte decomposition during extended battery cycling is an ongoing problem that leads to capacity fade, reduced charge/discharge rates, and shorter battery lifetimes [3–5]. In addition, uncontrolled SEI decomposition reactions at temperatures above roughly 80 °C can contribute to thermal runaway events and catastrophic battery fires [6–9].

As such, designing a durable, highly conductive, and stable SEI can significantly improve the power density, durability, and safety of LIBs for a range of applications. While a number of treatments, charging protocols, and chemical additives have been identified to increase the SEI's chemical and thermal stability [10–17], there is little ability to directly and quantitatively relate these techniques to the resulting SEI properties. In short, scientifically-guided design of stable SEI interfacial layers requires a better understanding of their elementary chemistry and structure, and how these properties vary with new materials, additives and operating procedures.

Significant attention has focused on the composition of the SEI using techniques such as TEM, AFM, XPS, FTIR, and NMR [1,3,18–35]. The SEI properties have been observed to be highly dependent on the electrolyte composition (solvent, salt, and additive compositions), the charging current and voltage, and the anode state of charge. Several studies have proposed a dual-layer structure, with a dense, inorganic inner layer adjacent to the anode and a porous, organic outer layer adjacent to the electrolyte [26,36–41]. However, there is still a need for greater chemical and spatial resolution to enable a truly mechanistic understanding of the SEI chemistry. For example, it is challenging to find a probe which is both sensitive to molecules rich in low-Z elements such as Li and is able to quantify chemical composition on the sub-nm scale, as is required to fully understand SEI chemistry.

Neutron Reflectometry (NR) measures the reflected intensity of a highly collimated neutron beam as a function of the grazing angle (or scattering vector  $Q_z$ ). Fitting NR data yields a high-resolution (on the order of 1 nm) 1D profile of the neutron scattering length density (SLD), which is a function of the local composition and density (see section 2.3). Because neutrons are highly penetrating and weakly interacting, NR is capable of operando measurements that do not alter the chemicals present in the sample. Combined with its sensitivity to isotopes and elements with low electron density (for example, hydrogen and natural Li contribute to very low SLDs, whereas high concentrations of deuterium and  $^6\text{Li}$  contribute to rather high SLDs), its high spatial resolution, and non-destructive nature, NR is particularly well suited for operando SEI studies.

Numerous studies over the past decade have demonstrated the validity and utility of NR for operando characterization of layered structures in LIBs, including the SEI [42–50]. Owejan et al. first used NR to quantify the SEI thickness and SLD on a non-intercalating Cu electrode. They observed large variations in the SLD (i.e. composition) and thickness (so-called ‘SEI breathing’) during a range of potentiostatic holds meant to mimic a charge-discharge cycle [42]. Veith and colleagues also observed this breathing phenomena via NR of the SEI on amorphous Si [47]. Veith and colleagues have used NR to thoroughly investigate a broad array of electrode-electrolyte interfaces, including on Si [48,49] and a high-voltage LMNO cathode [43]. While NR is a very useful probe for SEI analysis, it is also very challenging, and thus far no NR studies have definitively observed the two-layer SEI structure proposed in the literature.

Herein, we demonstrate parallel operando NR and electrochemical quartz crystal microbalance with dissipation monitoring (EQCM-D) measurements to directly quantify the structure and neutron SLD of an SEI formed on a non-intercalating tungsten anode. QCM-D measures the vibration frequency and dissipation of a piezoelectric crystal under a sinusoidal voltage input. The frequency shift can be used to determine SEI mass with high sensitivity ( $\sim 2 \text{ ng/cm}^2$ ) and time resolution

( $\sim 100 \text{ Hz}$ ). QCM-D has previously been combined with simultaneous electrochemical measurements (EQCM-D) to understand SEI formation dynamics [40,51–54]. Because the elementary chemistry of electrolyte reduction remains poorly quantified, a non-intercalating tungsten electrode is used for all experiments here, in order to isolate the NR, mass uptake, and electrochemical signal due to interfacial layer growth, separate from any intercalation-related artifacts. Subsequent work will extend these initial results to examine the impact of electrode material, electrolyte composition, and intercalation activity on relevant substrates such as carbon.

This study expands upon the previous NR measurements of the SEI on a non intercalating Cu electrode [42], improving the NR sensitivity via anode material selection and alternative electrolyte deuteration. Combined analysis of the data provides insights into the elementary chemistry during the initial stages of electrolyte reduction on this system. NR measurements directly observe a two-layer structure similar to that proposed for the SEI, including a dense, 3.7 [3.5, 4.0] nm thick inorganic inner layer and a porous, 15.7 [14.4, 17.9] nm thick organic outer layer. The layer mass was 1207.2 [1205.2, 1209.2]  $\text{ng/cm}^2$  after a series of 9 cyclic voltammetry (CV) cycles between 0.05 V and 1.45 V (vs  $\text{Li/Li}^+$ ). Throughout the manuscript, numbers in brackets represent 68% confidence intervals and error bars and  $\pm$  uncertainties represent one standard error. Results reveal two main reduction processes, one at  $\sim 0.75 \text{ V}$  and one at  $< 0.25 \text{ V}$  (vs.  $\text{Li/Li}^+$ ), with heavier molecules deposited during the former process. Correlating the parallel NR and EQCM-D results identifies SEI chemical composition which are consistent with the combined experimental data.

## 2. Experimental methods

### 2.1. Electrochemical control

For the NR and EQCM-D experiments below, a Reference 600 potentiostat (*Gamry Instruments*<sup>1</sup>) was used to control the electrochemical measurements. The measurement uncertainty of the potentiostat was  $\pm 1 \text{ mV}$  on all voltage measurements and  $\pm 0.2\%$  of the measured current. During NR experiments, the open circuit potential (OCP) was monitored continuously after cell assembly, with the cell at room temperature. During EQCM-D, cyclic voltamograms (CV) were used to grow an SEI on the sensor surface. Nine cycles were recorded at 10 mV/s between 0.05 and 1.5 V at a controlled temperature of 30 °C (all voltages in the paper are relative to  $\text{Li/Li}^+$ ).

### 2.2. NR cell fabrication

While our prior study pioneered NR as an in operando probe of SEI properties on a non-intercalating copper electrode [42], the effect of the SEI on the NR data was subtle. This is due to the relatively weak neutron scattering contrast between the SEI and adjacent layers, as compared to the much higher contrast between the Cu working electrode and its adjacent layers in the cited study. The current study employs a tungsten working electrode to reduce the dominating effects of the electrode-substrate contrast, and thereby improves the sensitivity of NR to the SEI (see Supporting Information).

Silicon wafers 76.2 mm in diameter and 5 mm thick (*El-Cat Inc.*) served as the substrate for the working and reference electrodes. The native oxide was removed from the working electrode via HF exposure (RCA cleaning), and then a roughly 10 nm thick dry thermal oxide was grown on the Si, to prevent spontaneous growth of tungsten silicides

<sup>1</sup> Certain commercial equipment, instruments, materials, suppliers, or software are identified in this paper to foster understanding. Such identification does not imply recommendation or endorsement by the National Institute of Standards and Technology, nor does it imply that the materials or equipment identified are necessarily the best available for the purpose.

and to prevent Si substrate lithiation. A ca. 15 nm thick tungsten film was then deposited via DC magnetron sputtering using a 76 mm diameter target at a controlled deposition current of 0.22 A (resulting in 80 W power) and an argon pressure of 0.12 Pa. On a separate 5 mm thick wafer, roughly 15 nm thick tungsten was sputtered directly onto the native SiO<sub>2</sub> and Lithium foil (*Sigma Aldrich*) was pressed onto the tungsten to act as the counter and reference electrode.

The two electrodes were electrically separated by a 500 μm thick Kalrez 4079 gasket, which is chemically compatible with the electrolyte. The gasket was affixed to the working electrode, and electrolyte was pipetted to form a meniscus in the 1.5-inch diameter hole in the gasket center. The electrolyte was 1 M (1 mol L<sup>-1</sup>) LiPF<sub>6</sub> salt (*BASF*, >99%) in a 1:1 (v/v) mixture of EC (*Alfa Aesar*, >99%) and deuterated DEC (d-DEC, *CDN Isotopes*, >99%). DEC solvent deuteration increases its SLD, providing better scattering contrast with the low SLD of the lithium-rich SEI. Trace water in the solvents was removed before mixing by adding 3 Å molecular sieves (*Sigma-Aldrich*) at 40 °C for two hours.

The counter electrode was then pressed onto the gasket, with aluminum foil leads between each electrode and the gasket for current collection. The electrodes and gasket were then clamped together between Al fronting and backing plates, as described previously [55]. All cell assembly work was done in a helium-filled glovebox. The NR compatible half-cell is shown schematically in Fig. 1 (a).

### 2.3. NR data collection and fitting

NR experiments were performed on the MAGIK instrument at the NIST Center for Neutron Research [56]. Our previous publications describe NR data collection in detail [42,55,57], but briefly: specular NR measures the reflected intensity of a collimated, monochromatic neutron beam scattered from the sample surface. Fitting the variations in reflected intensity as a function of scattering vector  $Q_z$  yields a one-dimensional depth profile of the sample SLD, which is a function of the sample composition. For a mixture of multiple phases (such as the SEI):

$$SLD = \sum_k V_k SLD_k \quad (1)$$

where  $V_k$  is the volume fraction and  $SLD_k$  the pure-phase SLD of phase  $k$ , summed over all phases present.

To characterize the substrate prior to electrochemical activity, the

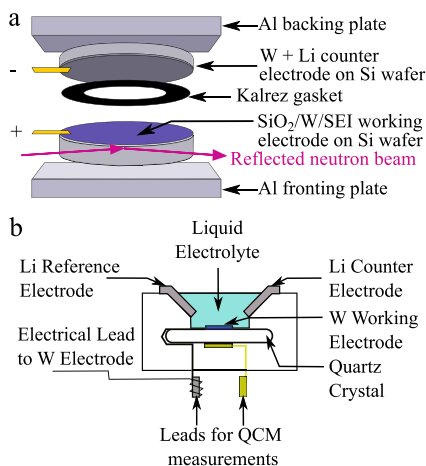


Fig. 1. Schematic of electrochemical cells. a) NR compatible half cell. Working and counter electrodes are deposited onto 5 mm thick polished Si wafers, which are clamped onto either side of a 500 μm thick Kalrez gasket to define the electrolyte volume. Spring-loaded Al fronting and backing plates are used for compression. b) The EQCM-D cell uses the Biolin Scientific open module. Strips of Li foil serve as counter and reference electrodes, while the QCM-D lead is used for electrical contact to the tungsten working electrode.

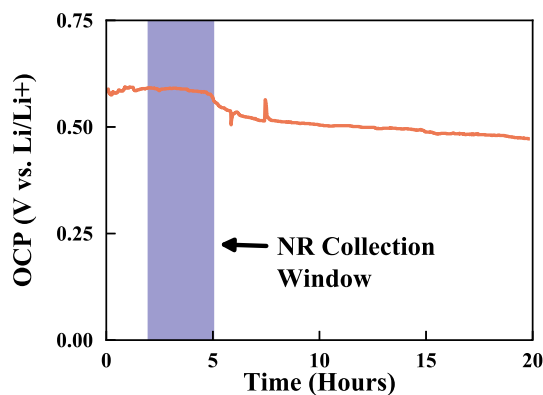


Fig. 2. OCP data taken during NR measurements. The low initial OCP and noisy decay over the course of the measurement indicates a moderate internal short. Only the NR data from the relatively stable OCP window indicated was used for analysis of the OCP condition.

tungsten working electrode was first isolated in a helium-filled aluminum can, and NR data was collected on the bare tungsten electrode (“W<sub>bare</sub>”). The electrolyte-filled cell in Fig. 1 (a) was then assembled and NR data was taken at OCP. As shown in Fig. 2, the measured OCP indicated unintentional shorting between the counter and working electrodes. The OCP was roughly 0.59 V for the first 5 h of the measurement, and decayed to roughly 0.48 V over the subsequent 15 h. NR fits were performed only on the data collected during the relatively stable OCP window, as indicated in the figure. At this potential an SEI formed on the tungsten, and this data set is labeled “W<sub>SEI</sub>.” To measure the electrode/electrolyte interface in the absence of any electrochemistry, a second electrolyte-filled cell, identical to the first except lacking any Li on the counter electrode, was assembled and measured with NR. This data set measures the chemical reactivity of the electrolyte and tungsten anode prior to reduction, and is labeled “W<sub>elyte</sub>.”

This study uses Refl1d [58] to fit the NR data. A model SLD profile is proposed as a layered structure of material “slabs,” each with three parameters: real and imaginary SLD (which are linked via the composition), thickness, and width of the interface with the next layer (i.e. the interfacial roughness and interdiffusion). The reflectivity of this model can then be calculated and evaluated against the measured data, using the  $\chi^2$  metric to maximize the model’s goodness-of-fit. A differential evolution algorithm (DREAM) randomly generates a large number of these models within a specified parameter space and allows this population to “evolve” over a user-defined number of generations. Because the probability of retaining a given parameter set is proportional to its likelihood, determined from  $\chi^2$ , the resultant population density represents the probability density. The approach therefore serves as a robust method to sample multi-dimensional parameter spaces without selecting only the nearest local minima (as can occur in gradient descent approaches), is able to identify multiple best fits when more than one solution is statistically feasible, and provides accurate uncertainty estimates for fitted parameters, as it explicitly preserves inter-parameter correlations.

Because the “W<sub>bare</sub>” and “W<sub>SEI</sub>” data sets were collected on the same sample, these data sets were fit simultaneously, defining common substrate fitting parameters (Si-SiO<sub>2</sub> interface width, SiO<sub>2</sub> thickness and SLD, and SiO<sub>2</sub>-W interface width) which were applied to both models. The SLD of the tungsten layer is allowed to vary to account for possible composition variations, which could result from a slightly porous W layer filled alternately with He, electrolyte, lithium, and/or SEI compounds, for example. Similarly, the tungsten layer thickness and interfacial width are allowed to vary between the two models. The W<sub>bare</sub> data was fit to a model with a surface layer at the W/vapor interface. The fitting process was repeated for zero, one, and two distinct layers at the electrode-electrolyte interface in the W<sub>SEI</sub> model. The interface

layer properties were allowed to vary over a wide range, to account for a range of possible layer thicknesses and compositions. The Bayesian Information Criteria (BIC) was used to discriminate between the different models [59–61].

A model was fit to the 'W<sub>elyte</sub>' data set which included the Si substrate, the SiO<sub>2</sub> thermal oxide, a tungsten electrode layer, and an electrolyte reservoir. Similar to the 'W<sub>bare</sub>'/'W<sub>SEI</sub>' fitting, this model was fit to the 'W<sub>elyte</sub>' data for models which proposed zero, one, two, or three distinct layers between the W and the electrolyte layers. Again, the BIC was used to differentiate between the competing models. The only constraint imposed for 'W<sub>elyte</sub>' relative to the 'W<sub>bare</sub>'/'W<sub>SEI</sub>' fits, was that the electrolyte relative density in 'W<sub>elyte</sub>' was constrained to be within  $\pm 2.5\%$  of that in the 'W<sub>SEI</sub>' fit. Other layer properties in 'W<sub>elyte</sub>' were allowed to vary independently from the 'W<sub>bare</sub>'/'W<sub>SEI</sub>' fitting results.

#### 2.4. EQCM-D measurements

EQCM-D measurements used the Q-Sense E1 system with QSX312 sensors (*Biolin Scientific*) which were 350  $\mu\text{m}$  thick AT-cut quartz crystals with a diameter of 14 mm, and a resonant frequency of 4.95 MHz. The electrode was a 300 nm thick tungsten layer with a surface roughness of less than 3 nm RMS and an active electrode diameter of 10.0 mm. The EQCM-D sensor was cleaned by sonication in a 2% sodium dodecyl sulfate solution at 40 °C for 30 min. The sensor was then rinsed with DI water and blown dry with N<sub>2</sub>. The QCM sensor/working electrode was installed in a Q-Sense open module, custom-fit to allow access for the Li foil counter and reference electrode (*Sigma Aldrich*), as shown schematically in Fig. 1(b). The electrolyte used was identical to that used for the NR measurements (see Section 2.3). Copper tape was attached to a pin on the bottom of the QCM module to provide the potentiostat with electrical access to the working electrode. The EQCM-D cell was assembled and tested in an argon-filled glove box, and the baseline resonant frequencies and dissipations for the sensor were calibrated in electrolyte. EQCM-D was measured at 30 °C using a range of harmonic overtones of the resonant frequency ( $n = 1-7$ ). In addition to the CV measurements described in Section 2.1, EQCM-D measured the SEI mass during a 5-h hold at 0.59 V, to estimate the mass grown during the short observed during NR.

#### 2.5. EQCM-D analysis

The QCM-D data was fit using both the viscoelastic Voigt model and the Sauerbrey model, using the volume-averaged density and viscosity of the electrolyte (1.26 g/cm<sup>3</sup> and 1.325 g/m<sup>1</sup>/s<sup>1</sup>, respectively) as parameters [62]. The viscoelastic model is generally more accurate than the commonly used Sauerbrey model [51,54,63,64] due to factors which violate the assumptions of the latter (e.g. SEI elasticity, SEI surface roughness, and the viscosity of the electrolyte) [40,65]. However, for the present data no differences were found between the viscoelastic and Sauerbrey models. A low-pass filter was used to reduce high-frequency noise in the fitted masses, using the MATLAB<sup>2</sup> 'designfilt' function with an order of 100 and a cutoff frequency of 10 mHz.

QCM-D data was correlated with the simultaneous CV data to calculate the mass per electron (m.p.e.) of the species deposited on the sensor surface during any given time period:

$$m.p.e = \frac{F\Delta m}{\Delta Q} \quad (2)$$

where  $F$  is Faraday's constant,  $\Delta m$  is the change in mass per area (g/cm<sup>2</sup>) measured during the specified window, and  $\Delta Q = -\int j dt$  is the charge per area (C/cm<sup>2</sup>) delivered to the sensor, with  $j$  equal to the current density (A/cm<sup>2</sup>) and  $t$  the time (s). After correcting for iR drop

and subtracting the capacitive double layer charging current from the measured currents, the m.p.e. was calculated here for electrode potentials < 1.1 V, using steps of 0.05 V to calculate  $\Delta m$  and  $\Delta Q$ . Calculated m.p.e. values can be compared to those for known SEI species to understand the layer formation dynamics as a function of deposition conditions [40,52,53].

### 3. Results and discussion

#### 3.1. Neutron reflectometry

Fig. 3 shows the NR data and SLD profiles for W<sub>bare</sub>, W<sub>elyte</sub>, and W<sub>SEI</sub>, and Table 1 lists the fitted parameter values. The thermal oxide and tungsten layer thicknesses closely match the target values, and agree well with auxiliary x-ray reflectometry measurements on a sacrificial witness sample deposited simultaneously with the tungsten working electrode. Additionally, the thickness, SLD, and interfacial widths for the thermal oxide agree very closely between the 'W<sub>bare</sub>'/'W<sub>SEI</sub>' sample and the 'W<sub>elyte</sub>' sample, despite a lack of any fitting constraints enforcing such agreement. Taken together with the low  $\chi^2$  values in Fig. 3(a), these results suggest good fits for all three models.

For sample W<sub>bare</sub>, the fitted tungsten layer density is slightly lower than the bulk value (95.2 [94.5, 95.5]% of bulk density). It was not possible to completely prevent exposure of the tungsten film to the atmosphere, and fitting reveals a thin surface layer in W<sub>bare</sub>. This is modeled as a porous tungsten tri-oxide (WO<sub>3</sub>, bulk SLD =  $4.1 \times 10^{-4} \text{ nm}^{-2}$ ). However, the low fitted SLD and thickness (which is near NR's resolution limit) could suggest that the layer represents an alternative tungsten oxide, a mixture of metallic and oxide phases, or is formed by other trace atmospheric contaminants.

Several differences are observed for the sample exposed to electrolyte but not electrochemically reduced (W<sub>elyte</sub>). The fitted SLD of the W layer increases slightly, relative to W<sub>bare</sub>. It was also observed that the thin, low-roughness oxide is not explicitly present in the model. However, the increased interfacial width is sufficient to mask a distinct, thin layer if it is still present. Above the W electrode there appears a thick two-layer interface structure with a nearly uniform SLD, which is slightly less than that of the electrolyte. Replacing the two layers with a single layer gives  $\chi^2 = 6.63$ . Omitting the interfacial layers entirely gives  $\chi^2 = 7.73$ . Due to the similar SLDs of the two layers (see Table 1) and the large interface width between the two layers (12.3 [10.1, 12.3] nm), it is referred to here as a single structure, the 'Pre-SEI'. Similar layers have been previously observed via neutron scattering techniques [42,50,66]. While the oxide is not explicitly included in the model, it could reside at the W-Pre-SEI interface. This is likely if the W layer of the sample were slightly thicker than that of the bare/SEI sample. In general, there are a number of possible interpretations of the pre-SEI composition that are consistent with the data, which are discussed in greater detail, below.

Holding at reducing potentials (W<sub>SEI</sub>) introduces several additional changes. The tungsten SLD is now lower than for either W<sub>bare</sub> or W<sub>elyte</sub> by roughly 1x or 2x the combined uncertainty of the fitted SLD, respectively. The surface oxide is no longer present, and the fitted thickness of the tungsten layer closely matches the summed thicknesses of the W + WO<sub>x</sub> layers in W<sub>bare</sub>. Most notably, a distinct bilayer structure is observed at the tungsten-electrolyte interface. This bilayer has a thin (3.68 [3.50, 4.00]nm) 'inner' layer with a low SLD adjacent to the tungsten, and a thicker (15.43 [14.74, 18.00]nm) 'outer' layer with an SLD which is closer to that of the electrolyte and consistent with that of the pre-SEI in W<sub>elyte</sub>. Alternate models which replaced this model with different numbers of interface layers ( $0 \leq n_{\text{layers}} \leq 4$ ) were also attempted, but gave inferior fits to the data (see Supporting Information).

Considering the three models in Fig. 3(b), four items merit discussion:

<sup>2</sup> The MathWorks, Inc; Natick, MA, USA; [www.mathworks.com](http://www.mathworks.com).

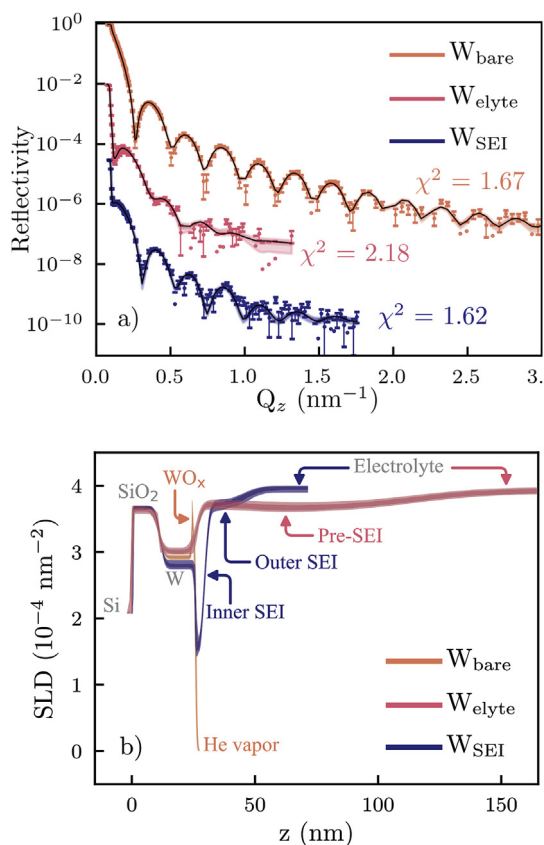


**Fig. 3.** NR results for tungsten in He vapor ( $W_{\text{bare}}$ ), in electrolyte prior to reduction ( $W_{\text{elyte}}$ ), and in electrolyte at reducing potential ( $W_{\text{SEI}}$ ). Solid lines and shaded regions represent best fits and 68% and 95% confidence intervals, respectively. (a) Reflectivity data and simulated NR from fitted models. Error bars represent  $\pm$  one standard deviation; (b) Fitted SLD profiles. Layer names corresponding to one particular model are color-coded to match that profile, while layers common to multiple models are colored grey. Due to the narrow confidence intervals, the best fits are omitted from the SLD profiles. (For interpretation of the references to color in this figure legend, the reader is referred to the Web version of this article.)

- 1. The fate of the  $W_{\text{bare}}$  surface oxide.** We observe that the surface layer in  $W_{\text{bare}}$  is explicitly present in neither the  $W_{\text{elyte}}$  nor the  $W_{\text{SEI}}$  data sets. For  $W_{\text{SEI}}$ , the fitted tungsten thickness increases, appearing to compensate for the thickness of the  $WO_x$  layer. However, given that the  $WO_x$  thickness is just below the resolution thickness of the technique, caution is required in understanding the fate of the  $WO_x$  layer. This is particularly true because the reflectivity data for  $W_{\text{SEI}}$  and  $W_{\text{elyte}}$  have a narrower  $Q_z$  range than  $W_{\text{bare}}$  (Fig. 3(a)). Given the low interface width, the low SLD of the inner SEI, and the fact that adding an additional layer at the W–SEI interface (Supporting Information) did not identify a surface oxide as being consistent with the NR data, it is likely that the  $WO_x$  layer has been removed in the  $W_{\text{SEI}}$  sample. However, similar conclusions are not fully supported for  $W_{\text{elyte}}$ , due to the high interface width between the W and Pre-SEI layers, the similarity between the  $WO_x$  and Pre-SEI SLDs, and the thin nature of the  $WO_x$  layer in  $W_{\text{bare}}$ . While the  $WO_x$  layer may have been consumed chemically upon exposure to the electrolyte, it is also altogether possible that the  $WO_x$  layer is still present at the interface with the Pre-SEI in  $W_{\text{elyte}}$ .
- 2. The composition of the Pre-SEI.** In addition to possibly containing  $WO_x$  components, the Pre-SEI SLD is also similar to that of the outer SEI in  $W_{\text{SEI}}$ , although the outer SEI is much thinner than the Pre-SEI (Fig. 3(b) and Table 1). It is currently unclear exactly how the composition of the Pre-SEI relates to that of the outer SEI. It is

**Table 1**

Fitted parameters for simultaneous fit to NR data taken in He vapor ( $W_{\text{bare}}$ ) in contact with electrolyte ( $W_{\text{elyte}}$ ), and after reduction in electrolyte ( $W_{\text{SEI}}$ ). Numbers in brackets represent 68% confidence intervals. The electrolyte reservoir is fit as a semi-infinite medium and as such has no fitted thickness.

Layer	$W_{\text{bare}}$	$W_{\text{elyte}}$	$W_{\text{SEI}}$
SiO <sub>x</sub>			
Thickness (nm)	11.05 [10.92, 11.13]	10.71 [10.55, 10.95]	Same as
SLD (10 <sup>-4</sup> nm <sup>-2</sup> )	3.67 [3.66, 3.68]	3.62 [3.61, 3.65]	$W_{\text{bare}}$
Tungsten			
Thickness (nm)	13.24 [12.98, 13.39]	15.94 [15.56, 16.09]	14.27 [14.13, 14.54]
SLD (10 <sup>-4</sup> nm <sup>-2</sup> )	2.92 [2.91, 2.94]	2.98 [2.98, 3.04]	2.81 [2.77, 2.83]
WO <sub>x</sub>			
Thickness (nm)	1.34 [1.30, 1.68]	–	–
SLD (10 <sup>-4</sup> nm <sup>-2</sup> )	3.89 [3.48, 3.89]	–	–
Pre-SEI: Layer 1			
Thickness (nm)	–	28.02 [20.50, 28.20]	–
SLD (10 <sup>-4</sup> nm <sup>-2</sup> )	–	3.66 [3.67, 3.75]	–
Pre-SEI: Layer 2			
Thickness (nm)	–	60.00 [59.00, 66.10]	–
SLD (10 <sup>-4</sup> nm <sup>-2</sup> )	–	3.63 [3.61, 3.70]	–
Inner SEI			
Thickness (nm)	–	–	3.67 [3.51, 4.02]
SLD (10 <sup>-4</sup> nm <sup>-2</sup> )	–	–	1.41 [1.36, 1.57]
Outer SEI			
Thickness (nm)	–	–	15.32 [14.67, 17.96]
SLD (10 <sup>-4</sup> nm <sup>-2</sup> )	–	–	3.72 [3.67, 3.76]
Electrolyte			
SLD (10 <sup>-4</sup> nm <sup>-2</sup> )	–	3.88 [3.89, 3.96]	4.00 [3.94, 3.99]

possible that the Pre-SEI represents a liganding layer that is only partially removed when the SEI was added, or removed entirely and replaced by a two layer SEI in  $W_{\text{SEI}}$ . It is also possible that the Pre-SEI is formed from preliminary electrolyte degradation products. In this case, it is plausible that a portion of the Pre-SEI is preserved and incorporated in the final SEI composition. Finally, the pre-SEI may also be the result of a systematic error in the fit. The current data is not able to differentiate between these interpretations as they are all consistent with the data.

- 3. Tungsten SLD variations.** The W SLD varies slightly between all three fits (Fig. 3(b) and Table 1). However, the 68% confidence intervals nearly overlap between all three models, and the most likely explanation is that the SLD variations represent systematic errors in the experiment and fitting procedures (for example, lateral inhomogeneities in the SEI or an interfacial gradient between layers that is not well approximated by the erf function used by Ref1d). An alternate explanation is that the W film is slightly porous in the  $W_{\text{bare}}$  condition (the fitted SLD is 95.1 [94.6, 95.6]% of the bulk tungsten SLD) and is filled with different materials in  $W_{\text{elyte}}$  and  $W_{\text{SEI}}$ . Filling 25% of the available pores with the electrolyte in  $W_{\text{elyte}}$  (SLD =  $3.88 \times 10^{-4} \text{ nm}^{-2}$ ) gives a tungsten layer SLD of  $2.97 \times 10^{-4} \text{ nm}^{-2}$ , which is close to the fitted value for  $W_{\text{elyte}}$  (Table 1). For  $W_{\text{SEI}}$ , filling all pores with Li (SLD =  $-0.88 \times 10^{-4} \text{ nm}^{-2}$ ) reduces the tungsten layer SLD to  $2.88 \times 10^{-4} \text{ nm}^{-2}$ , which is similarly close to the fitted value.
- 4. The nature of the SEI.** Two factors might prevent us from directly labeling the interfacial bilayer in the SLD profile of  $W_{\text{SEI}}$  (Fig. 3(b)) as an SEI. One is the uncontrolled electrochemistry in this partially-shorted  $W_{\text{SEI}}$  sample. The other is the possible initial presence of a surface tungsten oxide in  $W_{\text{bare}}$ , which can store lithium via the conversion reaction:



The NR data on  $W_{\text{elyte}}$  helps to determine whether or not the interfacial structure in  $W_{\text{SEI}}$  could have been formed by non-electrochemical means (i.e., whether or not it is truly an SEI). The absence of the thin, low-SLD layer in  $W_{\text{elyte}}$  (Fig. 3(b)) confirms that the layers in  $W_{\text{SEI}}$  are formed from electrochemical activity and not chemical reactions with the electrolyte. As mentioned above, the thick Pre-SEI in  $W_{\text{elyte}}$  could correspond to a carbonate/hydroxide liganding layer, similar to that observed in previous studies [42,50], or could be related to the ‘outer’ layer in  $W_{\text{SEI}}$ .

Several other observations support the conclusion that the observed bilayer is an SEI. First, the observed dual-layer structure is very similar to findings in literature [26,36–41], and the inner layer is similar to that observed by Owejan et al. [42], with a similar thickness (3.67 [3.50, 4.02] nm), and a relatively low SLD. The SLD here is slightly lower than in that study, which is consistent with protonation of the EC electrolyte solvent in this study, vs. the deuterated EC in that study (since the SEI is expected to be composed primarily of EC decomposition products [67,68]). The inner layer SLD suggests that it is composed of lower-SLD inorganic compounds such as LiOH ( $0.06 \times 10^{-4} \text{ nm}^{-2}$ ),  $\text{Li}_2\text{O}$  ( $0.812 \times 10^{-4} \text{ nm}^{-2}$ ), LiF ( $2.301 \times 10^{-4} \text{ nm}^{-2}$ ) and Li ( $-0.88 \times 10^{-4} \text{ nm}^{-2}$ ). Additionally, the high SLD contrast between the electrolyte and this layer suggest that it is fairly dense.

The outer layer is thicker (15.74 [14.40, 17.96] nm) and has an SLD quite close to that of the electrolyte, which suggests it is porous and/or composed of high-SLD organic compounds such as LEDC ( $(\text{CH}_2\text{OCO}_2\text{Li})_2$ ) and deuterated lithium ethyl carbonate (d-LEC) (SLDs estimated at  $2.95 \times 10^{-4} \text{ nm}^{-2}$  and  $8.66 \times 10^{-4} \text{ nm}^{-2}$ , respectively). LEDC is widely proposed as one of the primary components of the overall SEI [18,25,34,68,69], and LEC has been observed as the primary reduction component of DEC [69].

This bilayer is henceforth referred to as the SEI. This study represents one of the first direct observations of the two-layer SEI structure proposed in the literature.

### 3.2. EQCM-D

Fig. 4(a) and (b) show the EQCM-D data (CV and mass uptake) during 9 CV sweeps between 0.05 and 1.5 V. During the first sweep, reduction peaks are observable at 800 mV and 275 mV, and a single oxidation peak is observed at 1.0 V. While the potential window shown here is narrower, the voltammetric profile is very similar to that previously measured on a Cu anode [42]. The peak at 800 mV is attributed to reduction of electrolyte solvents, which is expected to begin at approximately 1.2 V and continue for the remainder of the cathodic sweep. The large increase in current magnitude below 0.5 V corresponds to additional SEI formation, while the reduction peak at 275 mV is likely due to underpotential deposition (UPD) of lithium [53]. The mass uptake curves in Fig. 4(b) are marked by significant mass uptake at potentials below 800 mV for all cycles, and a slight reduction in SEI mass during positive-going sweeps at potentials above roughly 1.0 V.

The passivating effect of the SEI is clearly observed by the decreasing current and mass deposition with increasing number of cycles. As shown in Fig. 4b, the net mass change per cycle is greatly reduced by the fifth cycle, going from 265.4  $\text{ng}/\text{cm}^2$  during cycle one to 100.4  $\text{ng}/\text{cm}^2$  during cycle five, and leveling off thereafter. These mass changes are quantified in Table 2, and are separated into low (below 1.0 V) and high (above 1.0 V) potential regimes in Table 3. The decrease in mass during each oxidation sweep is attributed both to the stripping of the Li UPD layer and partial dissolution of the reduction products into the electrolyte. This is consistent with the findings of our previous study [42]. As seen in Table 3, the differential mass increase (below 1.0 V) is highest during the first cycle and continually decreases in magnitude in each cycle thereafter. The mass loss above 1.0 V begins at 30.4  $\text{ng}/\text{cm}^2$  during cycle 1, increases in magnitude to 54.1  $\text{ng}/\text{cm}^2$  during cycle 5, and then reaches a final value of 23.6  $\text{ng}/\text{cm}^2$  during cycle 9.

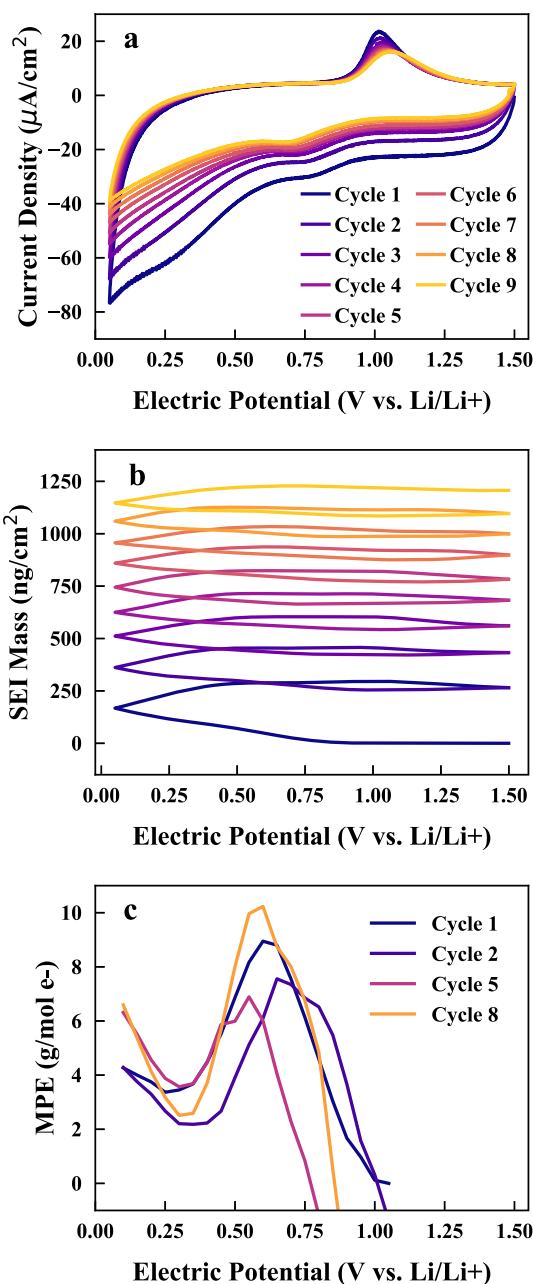


Fig. 4. EQCM-D results showing current and mass changes on a non-intercalating tungsten electrode during CV sweeps between 0.05 V and 1.5 V vs. Li/Li+ (sweep rate: 10 mV/s). (a) Current; (b) Mass; (c) Mass per electron (m.p.e.) for representative negative-going sweeps.  $T = 30^\circ\text{C}$ .

Finally, as shown in the Supporting Information, the SEI viscosity and shear suggest a film that becomes more rigid during the CV measurements. The viscosity is 0.0  $\text{kg}/\text{m}^2/\text{s}$  at the beginning of the experiment, and increases to  $4.1 \times 10^{-2} \text{ kg}/\text{m}^2/\text{s}$  by the end of the ninth cycle. The shear begins at  $6.3 \times 10^{12} \text{ Pa}\cdot\text{s}$ , and decreases to  $7.7 \times 10^6 \text{ Pa}\cdot\text{s}$  by the experiment's end.

Fig. 4(c) shows the m.p.e. for selected negative-going sweeps, calculated via Eq. 2. The results show three main trends, with respect to the electrode potential during the negative-going sweep. The m.p.e. of the species deposited in the range of 0.5–0.75 V ranges from 6 to 10  $\text{g}/\text{mol}$  of electron. Below roughly 0.6 V the m.p.e. decreases to a minimum at roughly 0.35 V, in the range of 2–4  $\text{g}/\text{mol}$  of electron. Finally, below 0.35 V, the m.p.e. increases with decreasing voltage, to 4–7  $\text{g}/\text{mol}$  of electron at the terminal voltage of 0.05 V.

**Table 2**

Total mass and mean m.p.e for each negative-going sweep in the CV of Fig. 4. Uncertainty on all mass values equals  $\pm 2$  ng/cm<sup>2</sup>.

Cycle	$m_{\text{tot}}$ at cycle end (ng/cm <sup>2</sup> )	$\Delta m$ during negative sweep (ng/cm <sup>2</sup> )	m.p.e during negative sweep (g/mole e <sup>-</sup> )
1.0	265.4	167.5	3.95
2.0	432.8	96.3	3.09
3.0	560.7	78.7	3.18
4.0	682.6	64.4	3.03
5.0	783.0	62.2	3.22
6.0	898.8	76.6	4.53
7.0	999.9	58.0	4.00
8.0	1096.6	59.8	4.47
9.0	1207.2	50.5	4.28

**Table 3**

Mass changes during each CV cycle in Fig. 4 for low (<1.0 V) and high (>1.0 V) potential regimes. Uncertainty on all mass values equals  $\pm 2$  ng/cm<sup>2</sup>.

Cycle	$\Delta m < 1.0$ V (ng/cm <sup>2</sup> )	$\Delta m > 1.0$ V (ng/cm <sup>2</sup> )
1.0	295.8	-30.4
2.0	201.6	-34.2
3.0	181.7	-53.8
4.0	169.5	-47.5
5.0	154.6	-54.1
6.0	148.6	-32.8
7.0	137.2	-35.9
8.0	126.5	-29.8
9.0	134.2	-23.6

**Table 4**

Theoretical m.p.e. values for expected SEI component molecules, based on molecular weight and number of Li atoms.

Compound	m.p.e (g/mol e <sup>-</sup> )
Li	7
Li <sub>2</sub> O	15
LiO <sub>2</sub>	19
LiOH	24
LiF	26
Li <sub>2</sub> CO <sub>3</sub>	37
(CH <sub>2</sub> OCO <sub>2</sub> Li) <sub>2</sub>	81

Assuming charge neutrality in the SEI, the theoretical m.p.e. for a given SEI component is calculated by dividing its molecular mass by the number of lithium atoms in that product. Table 4 lists several common SEI components and their theoretical m.p.e values. Comparing the values in Table 4 with those in Fig. 4(c), it is apparent that the measured m.p.e. values are well below the theoretical values for any of the expected products. The maximum value observed in Fig. 4(c) is in the range of 7–10 g/mol of electron. While this matches most closely with lithium deposition, lithium UPD is expected to occur at lower potentials. The most likely explanation for this discrepancy is that there is a low current efficiency for SEI deposition (i.e. the total current delivered was greater than that required to grow the observed SEI). This suggests that a majority of the reduction products were not retained within the SEI; either they form directly in the electrolyte and are never part of the SEI, or are deposited initially in the SEI but are soluble in the electrolyte. This is consistent with our previous NR work, in which the ratio of the measured charge to the modeled charge (i.e. that required to form

the SEI measured by NR) ranged between 1.85 and 5.39 [42].

Due to the unknown current efficiency for SEI deposition, the results in Fig. 4(c) provide only qualitative insight into the SEI formation chemistry. Regardless, there are several important conclusions from the m.p.e. analysis. First, assuming that the fraction of the total current resulting in net SEI deposition does not vary significantly as a function of potential, it is noted that heavier species (likely the organic molecules listed in Table 4) are deposited at 0.75 V, with lighter (likely inorganic) species formed at lower potentials. Additionally, we observe that the m.p.e. for reduction processes below 0.25 V is larger for later cycles than for the initial cycles. This is consistent with the trends in Table 2, in which the m.p.e. is in general greater for later cycles than for earlier cycles. Again, it cannot be determined from the present data whether this indicates a shift in the electrolyte reduction mechanism for later cycles, or an increase in the deposition efficiency of SEI products.

### 3.3. Quantifying the SEI chemical composition

To better quantify the range of possible SEI compositions consistent with the NR and EQCM-D data, a Monte Carlo (MC) composition fitting tool was developed for this study. This method leverages the Bayesian approach to NR fitting in the Refl1d software for quantitative analysis of the chemical composition of the SEI, given the mass, thickness, and SLD data.

The modeling tool's logic is illustrated in Fig. 5. The routine generates a random SEI model, which includes layer thicknesses and volume fractions of likely SEI compounds for both the inner and outer layers. Each layer thickness is independently chosen randomly from a normal distribution having the same 68% confidence interval as the NR fit. The volume fractions are chosen as a random array of  $k$  elements (one for each possible layer component), and then normalized so that the volume fractions sum to 1.0 for each layer (inner and outer).

The probable SEI components were based on previous literature [18,19,25,34,40,42,53,68]. The inner SEI is expected to contain mostly inorganic compounds, represented here by four components: Li<sub>2</sub>O, LiOH, Li<sub>2</sub>CO<sub>3</sub>, and LiF. The inner layer is also expected to contain Li from UPD and electrolyte due to porosity. Because LiOH is expected to form primarily from the reduction of trace water, its deuterated equivalent is not considered. The outer SEI is expected to be composed of organic compounds, and is proposed to contain LEDC and deuterated LEC, the primary reduction components of EC and deuterated DEC, respectively, and electrolyte from porosity. Even though evidence supports a primarily inorganic inner SEI and a primarily organic outer SEI, the models did not *a priori* make assumptions about any such division. Rather, the SEI composition model considered the possibility of organic components in the inner layer and inorganic components in the outer layer to evaluate the proposed segregation between layers.

For each proposed model, the inner and outer layer SLDs and the total SEI mass are calculated and compared to the NR and EQCM-D data, respectively, to select 'likely' models. A likely model is one that is consistent with the experimentally-determined inner layer SLD, outer layer SLD, and the total SEI mass. The posterior distributions from Refl1d for the inner and outer layer SLDs are used as an approximation of the probability distribution to calculate a mean and standard deviation for each layer SLD (assuming a normal distribution). By comparing a proposed model layer's SLD value to the respective probability distribution, it is possible to calculate the probability  $P$  of observing the layer SLD, given the NR data,  $P(SLD_{\text{model layer}} | SLD_{\text{NR}})$ . Likely models are identified via a modified Hastings-Metropolis algorithm: for each layer (inner or outer) of a model, a random number  $0 \leq N \leq 1$  is chosen, and the model is deemed likely if  $P(SLD_{\text{model layer}} | SLD_{\text{NR}}) > N$  for both the inner and outer layer. Because the NR and EQCM-D data were collected on different samples, with different sizes, and different reduction protocols (potentiostatic short vs. CV cycles), the EQCM-D data was used to generate a broad range of acceptable SEI mass values. The lower and upper limits were the mean SEI mass  $\pm$  one standard deviation, taken

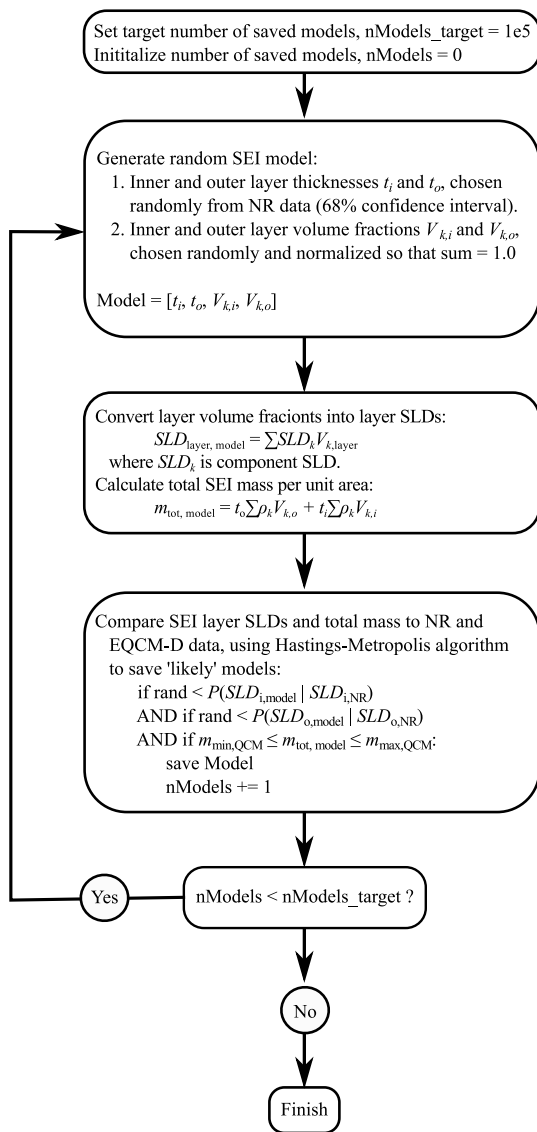


Fig. 5. Illustration of the logic used in the MC composition modeling tool. Random SEI composition models are generated and compared to the NR and EQCM-D data to select models which are consistent with the data. 'Likely' models are saved, until a set number of likely models have been identified.

from four sets of CV cycles. If the model SLDs were deemed likely and the model SEI mass fell within the acceptable range, the model was saved as a 'likely' model. This procedure continued until the number of 'likely' models identified exceeds a pre-selected target ( $1 \times 10^5$ , in this study). The modeling tool (and all other data and routines related to this manuscript) can be viewed and downloaded from the corresponding author's GitHub repository [70].

Histograms showing the volume fraction population distribution of each component for the inner and outer layers are shown in Figs. 6 and 7, respectively. Four aspects of the model merit discussion. First, it should be noted that the composition models are under-determined: there are sixteen total components, between the two layers, and only five constraining equations (the total SEI mass, the two layer SLDs, and the fact that the volume fractions must sum to 1.0 for each layer). Therefore, the model does not identify a 'best' fit, but rather identifies composition ranges which are consistent with the data.

Second, the volume fractions with the highest counts cannot strictly be considered the 'best' values. While matching the fitted SLDs more closely leads to a higher model probability and therefore should correlate with a high rate of observation in Figs. 6 and 7, a particular

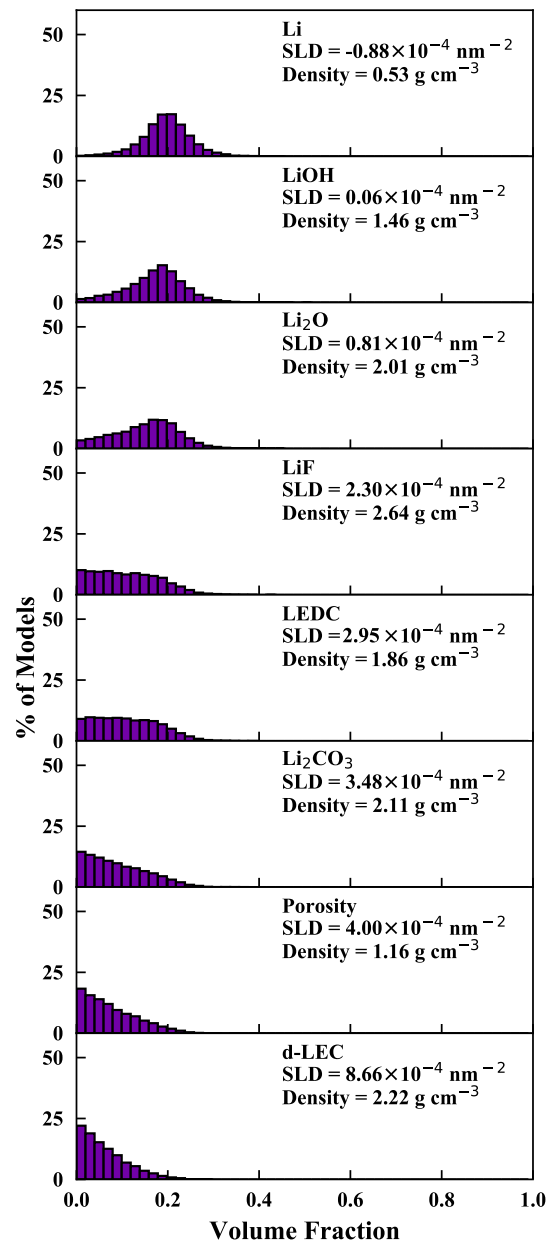


Fig. 6. Histograms of inner SEI component volume fractions which are consistent with both the NR and EQCM-D.

component volume fraction can still be observed at a high rate if it is part of many lower-probability models. That is, the very 'best' model (with the lowest  $\chi^2$  value) may be such that  $\chi^2$  is highly sensitive to the parameter values, such that even small changes in the neighborhood of the best fit are associated with large increases in  $\chi^2$  and therefore decreases in probability. In this case, the chances of identifying 'likely' models in the neighborhood of this 'best' model are low, such that the best fit might have a low count number in the Figs. 6 and 7 histograms. For a model which provides a poorer (but still sufficiently likely) fit to the SLDs, but where  $\chi^2$  is less sensitive to parameter variations, there may be a large number of models which are deemed likely, leading to a higher count rate in the histograms. Therefore, while the histograms can be considered roughly equivalent to a probability distribution–volume fractions with higher counts are more likely to be consistent with the data–caution is required in identifying a 'best' fit from the histograms.

Third, the model is explicitly unable to discriminate between components with similar SLD and density values. For example, the

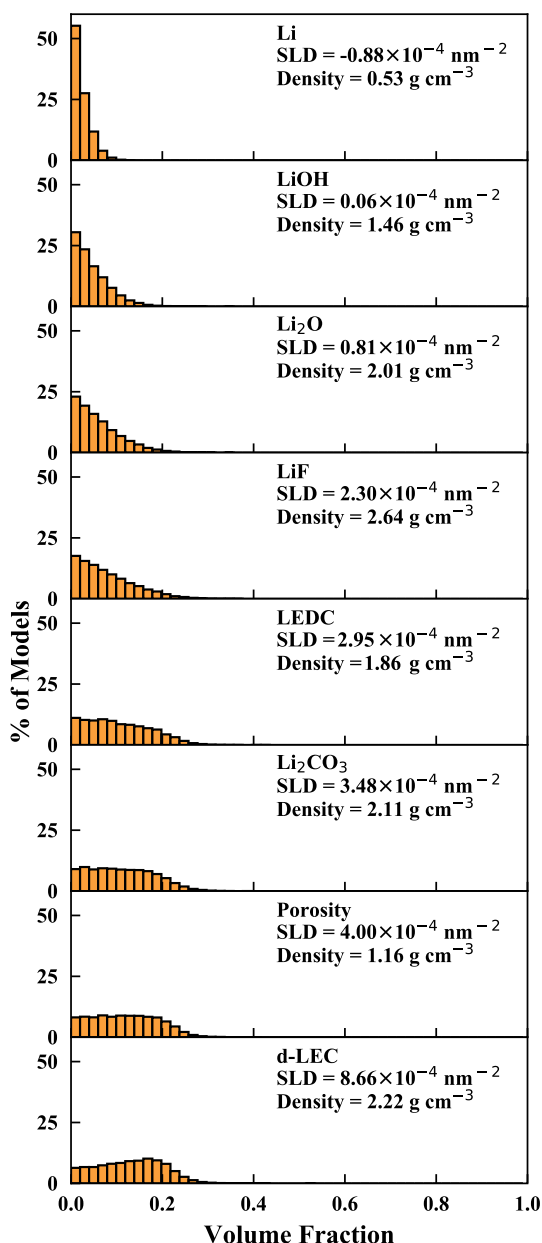


Fig. 7. Histograms of outer SEI component volume fractions which are consistent with both the NR and EQCM-D.

histograms for  $\text{Li}_2\text{CO}_3$  and LEDC, which have similar property values, look very similar, as do those for LiOH and  $\text{Li}_2\text{O}$ . The number of similar compounds included in the model will effect the overall scale of the volume fraction of those components.

Fourth, the histograms are highly sensitive to the components included. Certain components included in the layer models here (such as d-LEC in the inner layer or UPD Li in the outer layer) could reasonably be excluded from the model, resulting in slightly different model results. This is certainly a valid extension of this work, and will become valuable as the techniques in this study are further refined and additional complementary measurements are incorporated to further constrain the fits. At present, particularly due to the significant differences between the NR and EQCM-D protocols, the model is used only to identify compositions which are ‘more likely’ and ‘less likely.’

The components in Figs. 6 and 7 are presented in order of SLD (lowest to highest). Low-SLD components are more likely in the inner layer (Fig. 6) and higher-SLD components more likely in the outer layer (Fig. 7), consistent with the SLD profile in Fig. 3(b). For the inner layer

histograms, the lowest-SLD components (Li, LiOH, and  $\text{Li}_2\text{O}$ ) each have peaks at volume fractions of roughly 20%, but a majority of the acceptable models had volume fractions lower than 10% for the highest-SLD components ( $\text{Li}_2\text{CO}_3$ , electrolyte/pores, and deuterated LEC). In the outer SEI histogram, the high-SLD organic molecules have relatively uniform probabilities in the volume fraction range of 0–25%. The probability of observing the low-SLD inorganics in the outer layer is much lower. In particular, the probability of Li in the outer SEI is exceedingly low: more than half of the acceptable composition models had a volume fraction of 0%.

#### 4. Conclusions

This study presents NR and EQCM-D measurements to quantify the chemical composition and structure of the SEI grown on a non-intercalating tungsten anode. The study expands upon prior NR measurements to improve sensitivity to the SEI. Fitting the NR data determined the depth profile of the SEI SLD (which is, in turn, related to its composition), revealing a dual-layer SEI structure. This included a thin, dense inner SEI with a low SLD and a thick, porous outer SEI with a high SLD. While this structure has been suggested by numerous simulations, ex situ depth profiles, and viscoelastic modeling of QCM-D data, this study presents a direct, unambiguous, operando observation of the two-layer SEI structure. This was made possible by the enhanced NR sensitivity to the SEI in this study, due to the tungsten anode and selective deuteration of the electrolyte.

EQCM-D data during 9 potential cycles between 0.05 V and 1.50 V vs.  $\text{Li}/\text{Li}^+$  showed consistent SEI growth below 1.0 V, both during negative- and positive-going sweeps. The SEI growth per cycle was  $265.4 \text{ ng}/\text{cm}^2$  during the first cycle, but quickly dropped thereafter, demonstrating the passivating effect of the SEI. The mass uptake per cycle stabilized at roughly  $100 \text{ ng}/\text{cm}^2$  by the fifth cycle. Qualitative analysis of m.p.e. data showed two main processes: higher m.p.e. components deposited between 0.5 and 0.75 V, and lower m.p.e. components deposited below roughly 0.35 V. Due to the unknown current efficiency for SEI deposition (i.e. the total current delivered was greater than that required to grow the observed SEI), the absolute m.p.e. values of the deposited species cannot be determined. But assuming a roughly constant current efficiency would suggest that heavier species (i.e. organics) are deposited between 0.5 V and 0.75 V, and lighter inorganics are deposited below 0.35 V.

A Monte Carlo simulation identified SEI composition ranges consistent with the combined EQCM and NR data sets, which agree with the conventional understanding of the two-layer SEI structure. The inner SEI is a dense (low porosity) layer more likely to contain light inorganic compounds, with non-zero quantities (roughly 20% by volume) of Li metal, LiOH, and  $\text{Li}_2\text{O}$ . Smaller amounts of organics are also possible. The outer layer is more likely to contain electrolyte (higher porosity) and organic reduction products such as LEDC (EC reduction products), LEC (DEC reduction products), and lithium carbonate.

The measured m.p.e. values were lower than for expected SEI products, and were also lower than the compositions identified by the Monte Carlo model. This supports the idea that either the SEI partially dissolves during cycling, or a significant portion of the current density does not result directly in SEI growth. The low total m.p.e. of the EQCM experiment combined with the presence of LiF and  $\text{Li}_2\text{CO}_3$  in the SEI suggests that organic SEI compounds react with trace impurities in the electrolyte to form the passivating inner layer, while simultaneously releasing mass into the electrolyte as dissolved products. This study demonstrates the powerful capabilities of NR as an operando probe for quantitative analysis of the SEI electrochemistry and composition. The results lend new specific, quantitative rigor for the analysis of SEI formation and evolution mechanisms, and lay the groundwork for a promising array of follow-on studies to develop stable and low-impedance SEI layers. Based on the enhanced sensitivity to the SEI established here, future studies will extend this work for new insights into the effect

of electric potential, electrolyte composition and additives, anode composition, and extended cycling on the SEI properties.

## Acknowledgements

We would like to sincerely thank the following agencies for support of this work: the Office of Naval Research under grant #N00014-14-1-0059, Dr. Michele Anderson, program manager, and the Department of Energy under Early Career grant # DE-SC0018019, Dr. Pappan Thyagarajan, Program Manager. We would like to thank Dr. Eric Rus for useful discussions and for preparation of the tungsten thin film samples used in the NR measurements. Research was performed in part at the NIST Center for Nanoscale Science and Technology, and NR fitting utilized resources at the Center for High Performance Computing at the Colorado School of Mines.

## Appendix A. Supplementary data

Supplementary data to this article can be found online at <https://doi.org/10.1016/j.jpowsour.2018.11.093>.

## References

- [1] D. Aurbach, Review of selected electrode-solution interactions which determine the performance of Li and Li ion batteries, *J. Power Sources* 89 (2) (2000) 206–218.
- [2] Q. Wang, J. Sun, X. Yao, C. Chen, Thermal behavior of lithiated graphite with electrolyte in lithium-ion batteries, *J. Electrochem. Soc.* 153 (2) (2006) 329–333.
- [3] P. Verma, P. Maire, P. Novák, A review of the features and analyses of the solid electrolyte interphase in Li-ion batteries, *Electrochim. Acta* 55 (22) (2010) 6332–6341.
- [4] S. Phul, A. Deshpande, B. Krishnamurthy, A mathematical model to study the effect of potential drop across the SEI layer on the capacity fading of a lithium ion battery, *Electrochim. Acta* 164 (2015) 281–287.
- [5] M.B. Pinson, M.Z. Bazant, Theory of SEI formation in rechargeable batteries: capacity fade, accelerated aging and lifetime prediction, *J. Electrochem. Soc.* 160 (2) (2013) A243–A250.
- [6] A.M. Andersson, K. Edström, Chemical composition and morphology of the elevated temperature SEI on graphite, *J. Electrochem. Soc.* 148 (10) (2001) A1100.
- [7] H. Yang, X.D. Shen, Dynamic TGA-FTIR studies on the thermal stability of lithium/graphite with electrolyte in lithium-ion cell, *J. Power Sources* 167 (2) (2007) 515–519.
- [8] N. Choi, I.A. Profatlova, S. Kim, E. Song, Thermal reactions of lithiated graphite anode in LiPF<sub>6</sub>-based electrolyte, *Thermochim. Acta* 480 (1–2) (2008) 10–14.
- [9] M. Ryou, J. Lee, D. Jin, W. Kim, Y. Kyeong, J. Wook, J. Park, Y. Min, Effects of lithium salts on thermal stabilities of lithium alkyl carbonates in SEI layer, *Electrochim. Acta* 86 (2012) 259–263.
- [10] R. Wagner, S. Brox, J. Kasnatscheew, D.R. Gallus, M. Amereller, I. Cekic-Laskovic, M. Winter, Vinyl sulfones as SEI-forming additives in propylene carbonate based electrolytes for lithium-ion batteries, *Electrochem. Commun.* 40 (2014) 80–83.
- [11] A. Bordes, K. Eom, T.F. Fuller, The effect of fluoroethylene carbonate additive content on the formation of the solid-electrolyte interphase and capacity fade of Li-ion full-cell employing nano Si-graphene composite anodes, *J. Power Sources* 257 (2014) 163–169.
- [12] X. Chen, X. Li, D. Mei, J. Feng, M.Y. Hu, J. Hu, M. Engelhard, J. Zheng, W. Xu, J. Xiao, J. Liu, J.-G. Zhang, Reduction mechanism of fluoroethylene carbonate for stable solid-electrolyte interphase film on silicon anode, *ChemSusChem* 7 (2) (2014) 549–554.
- [13] R.W. Schmitz, P. Murmann, R. Schmitz, R. Müller, L. Krämer, J. Kasnatscheew, P. Isken, P. Niehoff, S. Nowak, G.-V. Röschenthaler, N. Ignatiev, P. Sartori, S. Passerini, M. Kunze, A. Lex-Balducci, C. Schreiner, I. Cekic-Laskovic, Investigations on novel electrolytes, solvents and SEI additives for use in lithium-ion batteries: systematic electrochemical characterization and detailed analysis by spectroscopic methods, *Prog. Solid State Chem.* 42 (4) (2014) 65–84.
- [14] C.C. Nguyen, B.L. Lucht, Comparative study of fluoroethylene carbonate and vinylene carbonate for silicon anodes in lithium ion batteries, *J. Electrochem. Soc.* 161 (12) (2014) A1933–A1938.
- [15] C. Xu, F. Lindgren, B. Philippe, M. Gorgoi, F. Björefors, K. Edström, T. Gustafsson, Improved performance of the silicon anode for li-ion batteries: understanding the surface modification mechanism of fluoroethylene carbonate as an effective electrolyte additive, *Chem. Mater.* 27 (7) (2015) 2591–2599.
- [16] K. Schroder, J. Alvarado, T.A. Yersak, J. Li, N. Dudney, L.J. Webb, Y.S. Meng, K.J. Stevenson, The effect of fluoroethylene carbonate as an additive on the solid electrolyte interphase on silicon lithium-ion electrodes, *Chem. Mater.* 27 (16) (2015) 5531–5542.
- [17] G.M. Veith, M. Doucet, R.L. Sacci, B. Vacaliuc, J.K. Baldwin, J.F. Browning, Determination of the solid electrolyte interphase structure grown on a silicon electrode using a fluoroethylene carbonate additive, *Sci. Rep.* 7 (1) (2017).
- [18] M. Nie, B.L. Lucht, Role of lithium salt on solid electrolyte interface (SEI) formation and structure in lithium ion batteries, *J. Electrochem. Soc.* 161 (6) (2014) A1001–A1006.
- [19] S.H. Kang, D.P. Abraham, A. Xiao, B.L. Lucht, Investigating the solid electrolyte interphase using binder-free graphite electrodes, *J. Power Sources* 175 (1) (2008) 526–532.
- [20] T. Yoshida, M. Takahashi, S. Morikawa, C. Ihara, H. Katsukawa, T. Shiratsuchi, J. Yamaki, Degradation mechanism and life prediction of lithium-ion batteries, *J. Electrochem. Soc.* 153 (3) (2006) A576.
- [21] I.A. Profatlova, S. Kim, N. Choi, Enhanced thermal properties of the solid electrolyte interphase formed on graphite in an electrolyte with fluoroethylene carbonate, *Electrochim. Acta* 54 (19) (2009) 4445–4450.
- [22] V.A. Agubra, J.W. Fergus, The formation and stability of the solid electrolyte interface on the graphite anode, *J. Power Sources* 268 (2014) 153–162.
- [23] S.-J. An, J. Li, C. Daniel, D. Mohanty, S. Nagpure, D.L. Wood, The state of understanding of the lithium-ion-battery graphite solid electrolyte interphase (SEI) and its relationship to formation cycling, *Carbon* 105 (2016) 52–76.
- [24] X.-B. Cheng, R. Zhang, C.-Z. Zhao, F. Wei, J.-G. Zhang, Q. Zhang, A review of solid electrolyte interphases on lithium metal anode, *Adv. Sci.* 3 (3) (2016) 1500213.
- [25] M. Gauthier, T.J. Carney, A. Grimaud, L. Giordano, N. Pour, H.-H. Chang, D.P. Fenning, S.F. Lux, O. Paschos, C. Bauer, F. Maglia, S. Lupart, P. Lamp, Y. Shao-Horn, Electrode–electrolyte interface in Li-ion batteries: current understanding and new insights, *J. Phys. Chem. Lett.* 6 (22) (2015) 4653–4672.
- [26] J. Zheng, H. Zheng, R. Wang, L. Ben, Lu, Liwei Chen, Liquan Chen, H. Li, 3d visualization of inhomogeneous multi-layered structure and youngs modulus of the solid electrolyte interphase (SEI) on silicon anodes for lithium ion batteries, *Phys. Chem. Chem. Phys.* 16 (26) (2014) 13229–13238.
- [27] Z. Zeng, W.-I. Liang, H.-G. Liao, H.L. Xin, Y.-H. Chu, H. Zheng, Visualization of Electrode/Electrolyte interfaces in LiPF<sub>6</sub>/EC/DEC electrolyte for lithium ion batteries via in situ TEM, *Nano Lett.* 14 (4) (2014) 1745–1750.
- [28] R.R. Unocic, L. Baggetto, G.M. Veith, J.A. Aguiar, K.A. Unocic, R.L. Sacci, N.J. Dudney, K.L. More, Probing battery chemistry with liquid cell electron energy loss spectroscopy, *Chem. Commun.* 51 (91) (2015) 16377–16380.
- [29] A. Tokranov, B.W. Sheldon, C. Li, S. Minne, X. Xiao, In situ atomic force microscopy study of initial solid electrolyte interphase formation on silicon electrodes for Li-ion batteries, *ACS Appl. Mater. Interfaces* 6 (9) (2014) 6672–6686.
- [30] R.L. Sacci, N.J. Dudney, K.L. More, L.R. Parent, I. Arslan, N.D. Browning, R.R. Unocic, Direct visualization of initial SEI morphology and growth kinetics during lithium deposition by in situ electrochemical transmission electron microscopy, *Chem. Commun.* 50 (17) (2014) 2104.
- [31] R.L. Sacci, J.M. Black, N. Balke, N.J. Dudney, K.L. More, R.R. Unocic, Nanoscale imaging of fundamental Li battery chemistry: solid-electrolyte interphase formation and preferential growth of lithium metal nanoclusters, *Nano Lett.* 15 (3) (2015) 2011–2015.
- [32] R.L. Sacci, J.L. Bañuelos, G.M. Veith, K.C. Littrell, Y.Q. Cheng, C.U. Wildgruber, L.L. Jones, A.J. Ramirez-Cuesta, G. Rother, N.J. Dudney, Structure of spontaneously formed solid-electrolyte interphase on lithiated graphite determined using small-angle neutron scattering, *J. Phys. Chem. C* 119 (18) (2015) 9816–9823.
- [33] B.L. Mehdi, J. Qian, E. Nasybulin, C. Park, D.A. Welch, R. Fallner, H. Mehta, W.A. Henderson, W. Xu, C.M. Wang, J.E. Evans, J. Liu, J.G. Zhang, K.T. Mueller, N.D. Browning, Observation and quantification of Nanoscale processes in lithium batteries by operando electrochemical (S)TEM, *Nano Lett.* 15 (3) (2015) 2168–2173.
- [34] A.V. Cresce, S.M. Russell, D.R. Baker, K.J. Gaskell, K. Xu, In situ and quantitative characterization of solid electrolyte interphases, *Nano Lett.* 14 (3) (2014) 1405–1412.
- [35] A.L. Michan, G. Divitini, A.J. Pell, M. Leskes, C. Ducati, C.P. Grey, Solid electrolyte interphase growth and capacity loss in silicon electrodes, *J. Am. Chem. Soc.* 138 (25) (2016) 7918–7931.
- [36] J.G. Thevenin, R.H. Muller, Impedance of lithium electrodes in a propylene carbonate electrolyte, *J. Electrochem. Soc.* 164 (2) (1987) 273–280.
- [37] R. Jorn, R. Kumar, D.P. Abraham, G.A. Voth, Atomistic modeling of the electrode electrolyte interface in li-ion energy storage systems: electrolyte structuring, *J. Phys. Chem. C* 117 (8) (2013) 3747–3761.
- [38] S. Kim, A.C.T. Van Duin, V.B. Shenoy, Effect of electrolytes on the structure and evolution of the solid electrolyte interphase (SEI) in li-ion batteries: a molecular dynamics study, *J. Power Sources* 198 (20) (2011) 8590–8597.
- [39] P. Lu, S.J. Harris, Lithium transport within the solid electrolyte interphase, *Electrochem. Commun.* 13 (10) (2011) 1035–1037.
- [40] Z. Yang, M.C. Dixon, R.A. Erck, L. Trahey, Quantification of the mass and viscoelasticity of interfacial films on tin anodes using EQCM-D, *ACS Appl. Mater. Interfaces* 7 (48) (2015) 26585–26594.
- [41] S. Shi, P. Lu, Z. Liu, Y. Qi, L.G. Hector, H. Li, S.J. Harris, Direct calculation of li-ion transport in the solid electrolyte interphase, *J. Am. Chem. Soc.* 134 (37) (2012) 15476–15487.
- [42] J.E. Owejan, J.P. Owejan, S.C. DeCaluwe, J.A. Dura, Solid electrolyte interphase in li-ion batteries: evolving structures measured in situ by neutron reflectometry, *Chem. Mater.* 24 (11) (2012) 2133–2140.
- [43] J.F. Browning, K.L. Jungjohann, Y. Wang, W.E. Tenhae, J.K. Keum, D.L. Wood, G.M. Veith, In situ determination of the liquid/solid interface thickness and composition for the li ion cathode limn1.5ni0.5o4, *ACS Appl. Mater. Interfaces* 6 (21) (2014) 18569–18576.
- [44] B. Jerliu, L. Dörrer, E. Hüger, G. Borchardt, R. Steitz, U. Geckle, V. Oberst, M. Bruns, O. Schneider, H. Schmidt, Neutron reflectometry studies on the lithiation of amorphous silicon electrodes in lithium-ion batteries, *Phys. Chem. Phys.* 15 (20) (2013) 7777.
- [45] B. Jerliu, R. Steitz, V. Oberst, U. Geckle, M. Bruns, H. Schmidt, Volume expansion during lithiation of amorphous silicon thin film electrodes studied by in-operando

- neutron reflectometry, *J. Phys. Chem. C* 119 (19) (2014) 9395–9399.
- [46] Bujar Jerliu, Erwin Hüger, Michael Horisberger, Jochen Stahn, Harald Schmidt, Irreversible lithium storage during lithiation of amorphous silicon thin film electrodes studied by in-situ neutron reflectometry, *J. Power Sources* 359 (2017) 415–421.
- [47] G.M. Veith, M. Doucet, J.K. Baldwin, R.L. Sacci, T.M. Fears, Y. Wang, J.F. Browning, Direct determination of solid-electrolyte interphase thickness and composition as a function of state of charge on a silicon anode, *J. Phys. Chem. C* 119 (35) (2015) 20339–20349.
- [48] G.M. Veith, M. Doucet, R.L. Sacci, B. Vacaliuc, J.K. Baldwin, J.F. Browning, Determination of the solid electrolyte interphase structure grown on a silicon electrode using a fluoroethylene carbonate additive, *Sci. Rep.* 7 (1) (2017).
- [49] T.M. Fears, M. Doucet, J.F. Browning, J.K.S. Baldwin, J.G. Winiarz, H. Kaiser, H. Taub, R.L. Sacci, G.M. Veith, Evaluating the solid electrolyte interphase formed on silicon electrodes : a comparison of ex situ x-ray photoelectron spectroscopy and in situ neutron reflectometry, *Phys. Chem. Chem. Phys.* 18 (20) (2016) 13927–13940.
- [50] H. Kawaura, M. Harada, Y. Kondo, H. Kondo, Y. Suganuma, N. Takahashi, J. Sugiyama, Y. Seno, N.L. Yamada, Operando measurement of solid electrolyte interphase formation at working electrode of li-ion battery by time-slicing neutron reflectometry, *ACS Appl. Mater. Interfaces* 8 (15) (2016) 9540–9544.
- [51] D.A. Buttry, M.D. Ward, Measurement of interfacial processes at electrode surfaces with the electrochemical quartz crystal microbalance, *Chem. Rev.* 92 (6) (1992) 1355–1379.
- [52] D. Aurbach, M. Moshkovich, Y. Cohen, A. Schechter, The study of surface film formation on noble-metal electrodes in alkyl carbonates/li salt solutions , using simultaneous in situ AFM , EQCM , FTIR , and EIS, *Langmuir* 15 (9) (1999) 2947–2960.
- [53] M. Moshkovich, Y. Gofer, D. Aurbach, Investigation of the electrochemical windows of aprotic alkali metal (Li, Na, K) salt solutions, *J. Electrochem. Soc.* 148 (4) (2001) E155–E167.
- [54] H. Tavassol, J.W. Buthker, G.A. Ferguson, L.A. Curtiss, A.A. Gewirth, Solvent oligomerization during SEI formation on model systems for Li-Ion Battery Anodes, *J. Electrochem. Soc.* 159 (6) (2012) A730–A738.
- [55] S.C. DeCaluwe, B.M. Dhar, L. Huang, Y. He, K. Yang, J.P. Owejan, Y. Zhao, A.A. Talin, J.A. Dura, H. Wang, Pore collapse and regrowth in silicon electrodes for rechargeable batteries, *Phys. Chem. Chem. Phys.* 17 (17) (2015) 11301–11312.
- [56] J. Dura, D. Pierce, C. Majkrzak, N. Maliszewskij, D. McGillivray, M. Loesche, K. O'Donovan, M. Mihailescu, U. Perez-Salas, D. Worcester, S. White, AND/R: advanced neutron diffractometer/refractometer for investigation of thin films and multilayers for the life sciences, *Rev. Sci. Instrum.* 77 (2006) 074301.
- [57] J.A. Dura, E.D. Rus, P.A. Kienzle, B.B. Maranville, Nanolayer analysis by neutron reflectometry, in: T. Imae (Ed.), *Nanolayer Research Methodology and Technology for Green Chemistry*, Elsevier, New York, 2017 (chapter 5).
- [58] P.A. Kienzle, J.A. Krycka, N. Patel Refl1d, Interactive depth profile modeler, <http://www.reflectometry.org/danse/software>.
- [59] G. Schwarz, Estimating dimensions of a model, *Ann. Stat.* 6 (2) (1978) 461–464.
- [60] M. Bogdan, J.K. Ghosh, R.W. Doerge, Modifying the Schwarz Bayesian information criterion to locate multiple interacting quantitative trait loci, *Genetics* 167 (2) (2004) 989–999.
- [61] S.C. Decaluwe, P.A. Kienzle, P. Bhargava, M. Baker, J.A. Dura, Phase segregation of sulfonate groups in nafion interface lamellae, quantified via neutron structures, *Soft Matter* 10 (31) (2014) 5763–5776.
- [62] M. Ue, Y. Sasaki, Y. Tanaka, M. Morita, Nonaqueous electrolytes with advances in solvents, in: T.R. Jow, K. Xu, O. Borodin, M. Ue (Eds.), *Electrolytes for Lithium and Lithium-ion Batteries*, Springer, New York, 2014, pp. 93–165 (chapter 2).
- [63] G. Sauerbrey, Verwendung von schwingquarzen zur wägung dünner schichten und zur mikrowägung, *Eur. Phys. J. A* 155 (1959) 206–222.
- [64] Jouko Kankare, Sauerbrey equation of quartz crystal microbalance in liquid medium, *Langmuir* 18 (18) (2002) 7092–7094.
- [65] B.D. Vogt, E.K. Lin, W.L. Wu, C.C. White, Effect of film thickness on the validity of the sauerbrey equation for hydrated polyelectrolyte films, *J. Phys. Chem. B* 108 (34) (2004) 12685–12690 aug.
- [66] G.M. Veith, L. Baggetto, R.L. Sacci, R.R. Unocic, W.E. Tenhaeff, J.F. Browning, Direct measurement of the chemical reactivity of silicon electrodes with LiPF<sub>6</sub>-based battery electrolytes, *Chem. Commun.* 50 (23) (2014) 3081–3084.
- [67] K. Xu, Whether ec and pc differ in interphasial chemistry on graphitic anode and how, *J. Electrochem. Soc.* 156 (2009) A751–A755.
- [68] G.V. Zhuang, K. Xu, H. Yang, T.R. Jow, P.N. Ross, Lithium ethylene dicarbonate identified as the primary product of chemical and electrochemical reduction of EC in 1.2 M LiPF<sub>6</sub>/EC:EMC electrolyte, *J. Phys. Chem. B* (2005) 17567–17573.
- [69] D.M. Seo, D. Chalasani, B.S. Parimalam, R. Kadam, M. Nie, B.L. Lucht, Reduction reactions of carbonate solvents for lithium ion batteries, *ECS Electrochem. Lett.* 3 (9) (2014).
- [70] [https://github.com/decaluwe/Tungsten\\_SEI\\_2018](https://github.com/decaluwe/Tungsten_SEI_2018).